NJC

Accepted Manuscript

This is an *Accepted Manuscript*, which has been through the Royal Society of Chemistry peer review process and has been accepted for publication.

Accepted Manuscripts are published online shortly after acceptance, before technical editing, formatting and proof reading. Using this free service, authors can make their results available to the community, in citable form, before we publish the edited article. We will replace this *Accepted Manuscript* with the edited and formatted *Advance Article* as soon as it is available.

You can find more information about *Accepted Manuscripts* in the Information for Authors.

Please note that technical editing may introduce minor changes to the text and/or graphics, which may alter content. The journal's standard Terms & Conditions and the Ethical guidelines still apply. In no event shall the Royal Society of Chemistry be held responsible for any errors or omissions in this *Accepted Manuscript* or any consequences arising from the use of any information it contains.

ROYAL SOCIETY OF CHEMISTRY

www.rsc.org/njc

Synthesis, Characterization and performance of ternary doped Cu-Ce-B/TiO_2 nanotubes on photocatalytic removal of nitrogen oxides

Rumin Li, Guojun Dong*, Guanmao Chen

College of Materials Science and Chemical Engineering, Key Laboratory of Superlight Materials and Surface Technology of Education Ministry, Harbin Engineering University, Harbin, 150001, China

Abstract: A series of single doped, co-doped and tri-doped TiO_2 nanotubes with Cu, Ce and B have been successfully prepared by hydrothermal method assisted by cetyl trimethyl ammonium bromide (CTAB). The photoelectrochemical properties of as-prepared samples were characterized by X-ray diffraction (XRD), transmissions electron microscopy (TEM), UV–vis absorbance spectroscopy, photoluminescence spectroscopy (PL), thermogravimetric analysis (TGA), X-ray photoelectron spectroscopy (XPS) and Fourier transform infrared spectroscopy (FT-IR). The doped TiO_2 nanotubes (TNTs) with different amounts of Cu, Ce and B were evaluated by the removal of nitride oxide under the irradiation of UV lamp to optimize the best doping concentration. The results show that Cu, Ce and B tri-doped TNTs exhibit the highest photocatalytic activity, which should be ascribed to the synergetic effect of narrowing the band-gap of TiO_2, which greatly inhibits the recombination of electrons and holes. The possible mechanism of photocatalytic reaction was also proposed.

Keywords: TiO_2 nanotubes; tri-doped; hydrothermal; synergetic effect; nitride oxide.

∗Corresponding author. E-mail address:dgj1129@163.com (Guojun Dong)

1. Introduction

Nitric oxide (NO) exhausted from waste incinerators, industrial boilers, engines, and automobiles can cause photochemical smog, acid rain, greenhouse effect and haze weather, which are harmful to the ecosystem and humanity [1-5]. Therefore, strict control of nitric oxide emission and removal processes was urgently needed. Various denitration processes, including combustion modifications, dry and wet processes have been put forward [6-10]. As an environmentally friendly and low cost method for removal of NO, photocatalyst has attracted an increasing attention [11,12].

Among various kinds of the photocatalysts, TiO_2 is the most widely used due to its high photocatalytic reactivity, better chemical and biological stability, non-toxicity, easy to prepare and economical availability [13]. However, the application of the photocatalysis has been restricted. The first reason is that the TiO_2 can only absorb ultraviolet (λ < 387 nm) due to its wide band gap (3.0-3.2 eV) [14]. Secondly, the photo-generated electron and hole pairs of TiO_2 are so easily to recombine resulting in a lower photo-quantum yield. Moreover, the low specific surface area of the conventional TiO_2 will result in a low photocatalytic efficiency. To address the visible light responsive TiO_2, numerous efforts have been made to find that doping nonmetal atoms, such as nitrogen [15], carbon [16], sulfur [17], phosphorus [18] and boron [19] in TiO_2, which can narrow its band gap and shift its optical response to the visible light region since the related impurity states are near the valence band edge. Changlin Yu et al.[20] have reported that the C-N-codoping TiO_2 samples exhibit much higher catalytic activities due to the synergetic effects in light absorption and suppression of

recombination of electron/holes pairs. In addition the C-N-codoping can decrease the ban-gap energy and promote the adsoption of visible light. Changlin Yu et al.[21] also reported that the Ag/TiO_2-B nanosquares has the high photocatalytic performance which should be attributed to the synergistic effects of B doping that narrows the band gap and the SPR of silver nanoparticles contribute to the highest activity. Furthermore, the single F or Ce-doped TiO_2 and the novel porous F, Ce-codoped TiO_2 have shown good mesoporous structures and the F, Ce-codoped TiO_2 exhibits much higher photocatalytic activity than pure and the single F or Ce-doped TiO_2. It was attributed that F doping which could produce more hydroxyl radicals inhibited the recombination of the photoinduced electrons and holes and Ce doping cause the wavelength response range of TiO_2 to the long wavelength region.[22] Compared with other nonmetals, the radius of the boron atom is very small and can site at an interstitial position, which replaces an O atom inducing some gap states close to the bottom of the conduction band, and thus leading to its visible light response activity.

Furthermore, great efforts have been devoted to prohibit the recombination of the photo-generated electrons and holes pairs. Transition metals and rare earths were the most promising candidates because of the possible transition of d and f orbital electrons, which can effectively reduce the recombination rate of electron-hole pairs and improve photo quantum yield. Transition metals such as Fe[23], W[24], Ag[25], Pt[26], Cu[27] and Zn[28] etc. were doped, which can introduce new energy levels to narrow its band gap. Out of all transition metals, copper ions as dopant attracted special attention due to copper species including Cu_2O and CuO can serve as the trap for charge

carriers and enhance the lifetime of electron-hole pairs [29]. Meanwhile, rare earth ions were considered as the ideal dopants because they can form complexes with various Lewis bases (organic acids, aldehydes, alcohols, thiols) in the interaction of the functional groups with their f orbital. Among rare earth elements, cerium is an excellent redox reaction catalyst and efficient electron acceptor which may trap photo-generated electrons and thereby increase the quantum yield. The different electronic structures of the Ce^{3+} with $4f^15d^0$ and Ce^{4+} with $4f^05d^0$ electronic transformation result in the shift of cerium oxide between CeO_2 and Ce_2O_3[30,31], which lead to different optical properties generating labile oxygen vacancies and bulk oxygen species to enhance the TiO_2 photocatalysis.

Compared with traditional TiO_2 particles, TiO_2 nanotubes (TiNTs) have the merits of large specific surface area, mesoporous structure, high aspect ratio, efficient electron conductivity and three-dimensional tubular structure, especially they can be used repeatedly and conveniently[32]. Currently, the modification of TiO_2 by co-doping has proved the most effective approach because of the synergetic effect and further enhancement of the visible light photoactivities. For instance, J. Xu et al.[33] prepared Ce, C-co-doped titania with a significant red-shift to visible region. Q. Wang et.al [34] reported that Gd, C, N and P quaternary doped anatase-TiO_2 have a high performance on the degradation of 4-chlorophenol, which was attributed to the synergetic effect of enhanced visible light absorption. However, Cu, Ce and B co-doped or tri-doped on TiO_2 nanotubes has rarely been reported.

In this work, a series of of Cu, Ce, B doped TiO_2 nanotubes were prepared

through a hydrothermal method, which was assisted by CTAB to modify the surface character of TiNTs to form mesopores on the shells [35]. The influence of Cu, Ce and B on the physicochemical properties of TiO_2 nanotubes was studied by several techniques. The photocatalytic activity was explored through the removal of NO under UV light. Moreover, the possible synergetic mechanism for the photocatalysis was also discussed.

2. Experimental section

2.1 Preparation of Cu-Ce-B/ TNTs

All analytical grade reagents, including $CuSO_4 \cdot 5H_2O$, $Ce(SO_4)_2 \cdot 4H_2O$, $NaBH_4$, NaOH, CTAB and anatase TiO_2 powder were used directly without further purification. In a typical synthesis, 1g of anatase TiO_2 was dispersed in 15 mL 10 mol $\cdot L^{-1}$ NaOH for 1 h under stirring. Subsequently, 0.21 g CTAB was added into the mixed solution and sonicated for 30 min. The mixture was then hydrothermally treated in a Teflon autoclave at 150 ^oC for 29 h. The obtained white powder (TiNT-Na) was rinsed with deionized water and ethanol several times, subsequently filtered in vacuum. After further washing with 0.1 mol $\cdot L^{-1}$ HCl, the material was finally rinsed with distilled water until neutral pH and dried at 120 ^oC, then calcined in air at 400 ^oC for 2 h to obtain pure TNTs.

Cu, Ce and B single-doped, co-doped and tri-doped TiNTs were synthesized by the similar process to TiNTs. In a brief procedure for the synthesis of Cu-Ce-B/TNTs, 0.2 at. % $CuSO_4 \cdot 5H_2O$, 0.3 at. % $Ce(SO_4)_2 \cdot 4H_2O$ and 2 at. % $NaBH_4$ were added to a beaker containing 10 mol $\cdot L^{-1}$ NaOH followed by ultrasonic-dispersion. Then 1 g

anatase TiO_2 and 0.21 g CTAB were added in the mixture, then transferred into a Teflon autoclave and heated at 150 ^oC for 29 h. The obtained product was washed with 0.1 mol L^{-1} HCl solution and distilled water until pH value was 7. The collected product was dried at 120 ^oC, and then calcined in air at 400 ^oC for 3 h to obtain Cu-Ce-B/TNTs. The TiO_2 coatings on glass board was obtained by coating the suspension on the glass followed by drying at 60 ^oC.

2.2 Characterization

The morphology and size of the samples were examined on a TEM (FEI Tecnai G^2 S-Twin) operated at 200 kV and HRTEM (H-7650, Hitachi LTD, Japan) at 120 kV. Energy-dispersive spectrum (EDS) analyzer was performed on a scanning electron microscope (SEM, JSM-6480). The crystalline phase of samples was examined by XRD (Rigaku D/max-IIIB) equipped with Cu Ka radiation (λ = 0.15405 nm) at 40 kV and 50 mA. The UV-Vis light absorption spectra were recorded by a TU-1901 spectrophotometer between 300-800 nm at room temperature. The photoluminescence (PL) spectra of the samples were measured with a UV-1601 spectrophotometer to obtain the recombination rates of the electron-holes pairs. The weight loss and thermal stability were determined on TGA-DSC (NETZSCH STA 409 PG/PC). X-ray photoelectron spectroscopy (XPS) measurements were performed on K-Alpha of Thermo Fisher Scientific with Al Kα radiation and the C_{1s} peak at 284.6 eV as reference. Fourier transform infrared (FT-IR) spectra were collected using a Nicolet 6700 spectrometer equipped with KBr beam splitter.

2.3 Photocatalytic test

The diagram of the experiment set is shown in Fig.1, which comprises the gas supply, UV photo-reactor and NO analytical system. Simulated gas with a flow of 100 mL/min was fed into the reactor using rotor flow meter controllers. In this work, NO gas was used as the target pollutant. NO, N_2 and O_2 (5%) were mixed to obtain the desired concentration of NO (150 ppm). The immobilized catalyst coated on a glass board was placed in the photo-reactor. Water vapor was obtained by passing dried air through a bottle containing deionized water at room temperature. The cylindrical photo-reactor (volume: ϕ300×100 mm) was irradiated with a UV lamp (8 W, Philips, the maximum light intensity: 365 nm). All the reactor and light source were operated in a dark chamber. The concentration of NO in the effluent gas was monitored by a ThermoStar Gas Analysis System GSD320 analyzer.

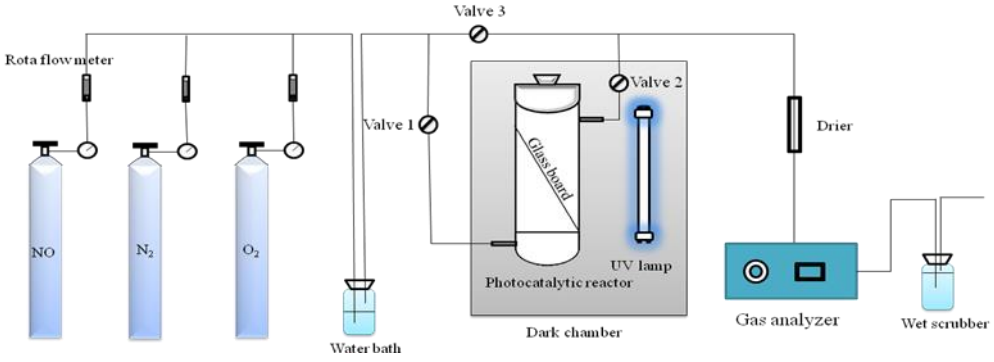

Fig. 1 Diagram of the photocatalytic equipment.

A preliminary test showed that there were no changes in the NO concentration observed when the valve 3 only opened after 30 min. The UV irradiation experiments were starting on when inlet and outlet NO concentration equalized. After the UV lamp was turned on, the NO and NO_2 concentrations were detected in the effluent gas stream. The removal efficiency of NO was calculated by as follow:

$$\eta(\%)=(NO_{in}-NO_{out})/\ NO_{in} \quad (1)$$

3. Results and discussion

3.1 XRD analysis

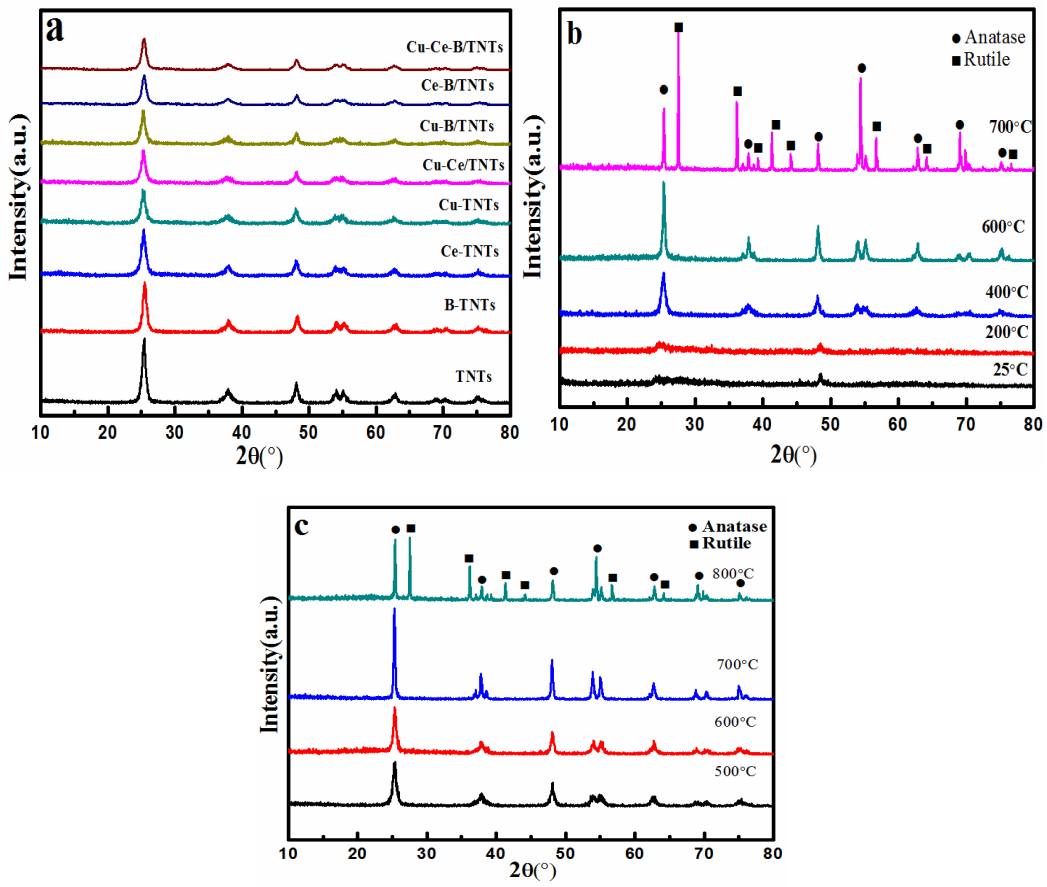

Fig. 2 XRD patterns of (a) pure TNTs, single doped, co-doped and tri-doped TNTs calcined at 400°C, (b) pure TNTs and (c) Cu-Ce-B/TNTs calcined at different temperature.

The XRD patterns of as-prepared TNTs with different dopants are presented in Fig.2a. The XRD results of the pure TNTs and the tri-doped TNTs calcined at different temperatures were observed in Fig.2b and Fig.2c. According to the Fig.2a, only the diffraction peaks of anatase TiO_2 can be observed for all samples. No other phases can be detected which can be due to high dispersion or the low amount of the doping element. Compared with the pure TNTs, Cu, Ce and B single doping results in broadening and decreasing intensity of the (101) peak, indicating the decreased crystallization of TiO_2 due to the weakened interaction of Ti-O bond. Furthermore,

Cu-Ce, Cu-B and Ce-B co-doping further increase the inhibitive trend. For the tri-doped samples, the trend is further enlarged. The average crystallite sizes, lattice distortion and crystal parameter of all samples are list in the Table 1. As shown, the average crystallite sizes of the single-doped samples decrease in the order of B, Cu and Ce, and in general terms, the co-doping and tri-doping further decrease the crystal average crystallite sizes. While the lattice distortion and crystal parameter of doping samples increase, implying that the doping atoms have been incorporated into the crystal lattice of TiO_2.

Fig.2b and 2c show the XRD patterns of TNTs and Cu-Ce-B/TNTs calcined at different temperatures, respectively. In Fig.2b, the characteristic peaks of titanate disappear which indicates that titanate decomposes into titanium dioxide when calcined from 25 ^oC to 400 ^oC, implying the phase transformation from noncrystalline to anatase. Furthermore, the diffraction peaks becomes stronger and narrower with the increment of calcination temperature. The diffraction peaks related with rutile phase arise when the temperature is enhanced to 700 ℃ for TNTs and 800 ℃ for Cu-Ce-B/TNTs, implying that the doping of Cu, Ce, and B inhibits the phase transformation from anatase to rutile.

Sample	*D* (nm)	ε (%)	*Crystal parameter*		
			a(=b)/nm	*c/nm*	*V*/(nm^3)
Pure TNTs	13.1	0.7197	0.3785	0.9514	0.1363
B	11.7	0.7750	0.3767	0.9509	0.1359
Cu	11.0	0.7541	0.3792	0.9540	0.1372
Ce	11.3	0.7958	0.3795	0.9545	0.1374
Cu-Ce	10.4	0.8453	0.3796	0.9574	0.1379

Cu-B	10.6	0.8431	0.3786	0.9535	0.1367
Ce-B	10.5	0.8436	0.3788	0.9538	0.1369
Cu-Ce-B	10.3	0.8523	0. 3798	0.9567	0.1380

Table 1 Physicochemical properties of as-prepared samples

3.2 TEM analysis

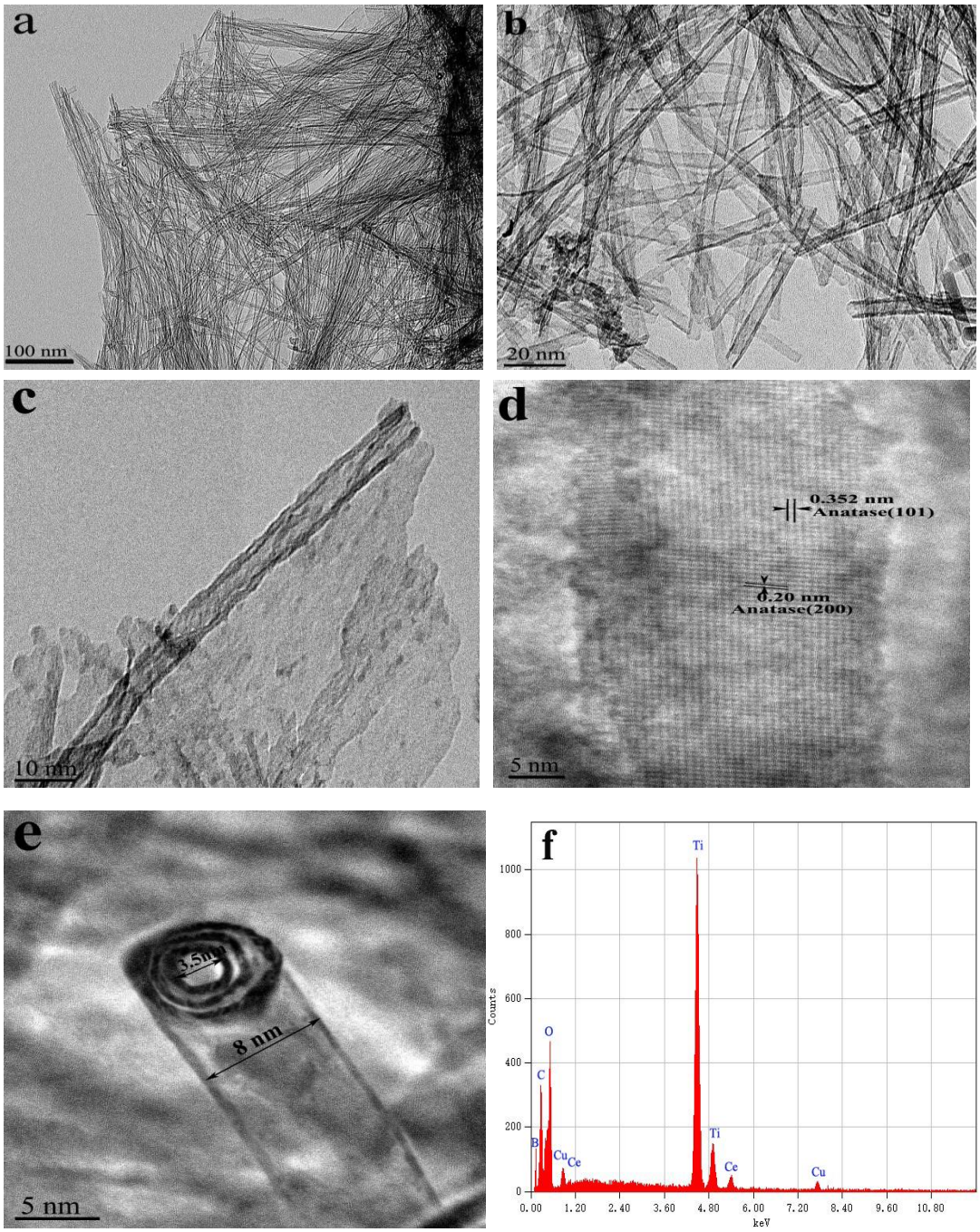

Fig.3 TEM image of Cu-Ce-B/TNTs (a, b), HRTEM images (c, d, e) and EDS spectrum of Cu-Ce-B/TNTs (f)

Fig.3 shows TEM and HRTEM images of Cu, Ce and B tri-doped TNTs prepared by the impregnated method. It can be clearly observed that the dopants of Cu, Ce and B have little effect on the morphology (Fig.3a and b). In Fig. 3e, the nanotubes exhibit multi-walled tubular structure of three layers with 8 nm outer and 3.5 nm inner diameters. Fig.3c shows the thin shells are curled up into a tube indicating the formation of TNTs. The Cu, Ce and B nanoparticles or clusters can not be observed on the surface, while the EDS spectrum (Fig.2f) confirms the existence of Cu, Ce and B elements in the product, which indicated that the doping atoms have incorporated into the crystal lattice of TiO_2. The HRTEM image (Fig.3d) also suggests single-crystalline nature of the anatase TiO_2. The interplanar distance of approximate 0.35 nm corresponds to the (101) plane of anatase TiO_2, which is consistence with the XRD result.

3.3 UV-Vis absorbance spectra analysis

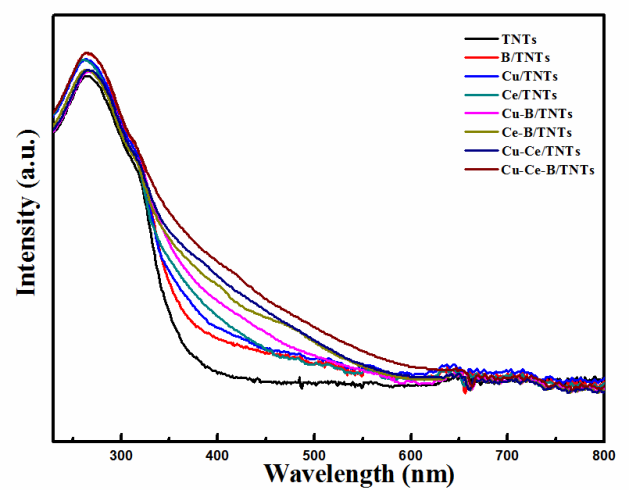

Fig. 4 UV-Vis absorbance spectra of pure TNTs, B/TNTs, Ce/TNTs, Cu/TNTs, Cu- B/TNTs, Ce-B/TNTs, Cu-Ce /TNTs and Cu-Ce-B/TNTs.

Fig.4 exhibits the UV-vis absorbance spectra of undoped, single doped, co-doped and trip-doped TNTs prepared by the co-impregnated method. It is clear that undoped

TNTs show absorption only in the UV region, and the absorption significantly shifts to longer wavelengths for single doped samples. In Table 2, the absorb edges and band gaps calculated from the absorb edges according to $E=hc/\lambda=1240/\lambda$($h=4.138\times10^{-15}$; $c=3.0\times10^{-17}$) increase. The incorporation of B with TiO_2 induces an obvious red shift and narrows the band gap energy. Guo et al.[30] reported that B replacing an O atom induces some gap starts close to the bottom of the valence band (VB) and this may be account for the red shift of the absorption edge in TiO_2, which is proved by the results in Table 2. Cu-doping leads to the red-shift of absorption edge significantly, indicating that the metal doping can form an impurity energy level within the band gap of TiO_2 to narrows its band-gap, and create oxygen vacancies due to the charge compensation effect to change the electronic structure of TiO_2 lattices. Ce-doping into TiO_2 leads to a significant shift towards higher wavelength, which should be ascribed to Ce^{4+}/Ce^{3+} ions as an electron scavengers to trap the electrons of TiO_2 and the Ce 4f level as a interfacial charge transfer and elimination of electron-hole recombination. Compared with the single doping, the absorption of the Cu-Ce, Cu-B, Ce-B co-doped TiO_2 are red shift due to the introduction of new energy levels by dopant species in the band gap of titania. The newly introduced energy levels narrow the conduction band of TiO_2 by Cu, Ce and the additional levels introduced by the B dopants near the valence band narrow the band gap of TiO_2, which make it become to red shift to the visible light range. As shown in Table 2, the dopant Cu, Ce and B can effectively narrow the band gap. Among all the doped samples, the biggest red shifted wavenumber and the lowest

band gap have been achieved for Cu-Ce-B/TNTs.

samples	TNTs	B	Cu	Ce	Cu-B	Ce-B	Cu-Ce	Cu-Ce-B
λ(nm)	387.5	418.4	429.3	446.8	465.3	480.1	483.4	502.4
E(eV)	3.20	2.96	2.89	2.78	2.66	2.58	2.56	2.47

Table 2 The absorb edge(λ) and band gap (E) of pure TNTs, B/TNTs, Ce/TNTs, Cu/TNTs, Cu-B/TNTs, Ce-B/TNTs, Cu-Ce /TNTs and Cu-Ce-B/TNTs.

3.4 PL properties analysis

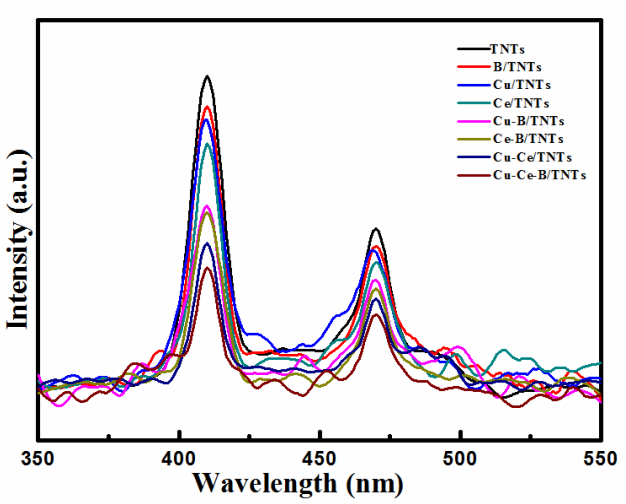

Fig. 5 PL spectra of pure TNTs, B/TNTs, Ce/TNTs, Cu/TNTs, Cu- B/TNTs, Ce-B/TNTs, Cu-Ce /TNTs and Cu-Ce-B/TNTs at the excitation wavelength of 300 nm.

The Fig.5 shows the PL spectra of the pure, single, co-doped, tri-doped TNTs prepared by co-impregnated method. The PL spectroscopy was used to investigate the separation efficiency of photo-induced electron/hole pairs and charge carrier lifetimes of semiconductors. As shown in Fig.5, the spectra of pure TNTs, single doped, co-doped and tri-doped excited at 300 nm have nearly similar curve shape except for the peak intensities. The strong peak at 410 nm was attributed to the band-edge free exciton luminescence while the peak at 470 nm belongs to the bound exciton luminescence. The PL emission spectra intensity of all the samples is in the order of:

TNTs < B-TNTs < Cu-TNTs < Ce-TNTs < Cu-B/TNTs < Ce-B/TNTs < Cu-Ce/TNTs < Cu-Ce-B/TNTs.

Generally, the lower PL intensity suggests the lower recombination electron–hole pairs, which leads to the high photocatalytic activity. The lowest intensity of Cu-Ce-B/TNTs among all the doped samples may be attributed to the electron transfer processes from the excited state (CB) to the new levels introduced by the metal and non-metal dopants.

3.5 TG-DSC analysis

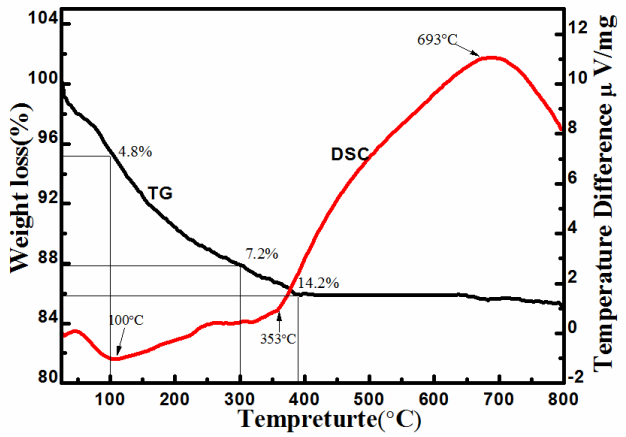

Fig.6 DSC–TG curves of Cu-Ce-B/TNTs samples

Fig. 6 shows the TG-DSC curves of Cu-Ce-B tri-doped TNTs. The TG curve of the sample mainly contains three stages. The first weight loss of 4.8% up to temperature 100 ^{o}C is attributed to the release of the physically absorbed water, which can be proved by an endothermic peak in the DSC curve at near 100 ^{o}C. The second weight loss of 7.2% occurs in the temperature range from 100 ^{o}C to 300 ^{o}C belongs to the evaporation or decomposition of the organic compounds like CTAB (boiling point 184-191 ^{o}C). The last stage weight loss from 300 ^{o}C to 400 ^{o}C is 2%, owing to the decomposition from titanate to titanium dioxide, and it is obvious in the DSC curve

that an transition exothermic peak appears near 353 °C. A weak exothermic peak at 693 °C in the DSC can be attributed to the phase transformation from antase to rutile, which is proved by XRD. No mass loss is observed when the calcination temperature is over 400 °C.

3.6 XPS analysis

The XPS spectrum of Cu-Ce-B/TNTs prepared by co-impregnated method is shown in Fig.7a, which indicates the peaks of Ti, O, Cu, Ce, B and C. The relative atomic concentration of Cu, Ce and B in estimated from the XPS data are 0.2 at.%, 0.3 at.% and 2 at.%, respectively. In the high-resolution XPS spectrum of Cu2p(Fig.7b), two components after the deconvolution of Cu 2p3/2 and Cu 2p1/2 correspond to copper species with different oxidation states. The broad peak around 932.6 eV with a shoulder peak can be fitted by two peaks at 932.0 eV and 933.4e V, the peak around 932.6 eV can be fitted at 951.5 eV and 953.1 eV. Based on the report [36], the peaks at 933.4 eV and 953.1 eV should be assigned to the Cu 2p3/2 peak and the Cu 2p1/2 peak of CuO. Meanwhile, a minor species of Cu appear at binding energies of Cu 2p3/2 and Cu 2p1/2 at 932.0 eV and 952.5 eV, respectively. This is ascribed to reduced copper species, namely, CuO would be reduced to Cu_2O. The results indicate that Cu species exist as Cu_2O and CuO in the TiO_2 nantobues.

In Fig.7c, the Ce3d XPS spectra can be fitted into ten peaks because of the multiple oxidation states (CeO_2 /Ce_2O_3) and hybrid orbital of Ce 4f and O 2p, which causes the splitting of peaks into doublets during the primary photoemission process. According to the established rule by Burroughs and Galtayries [37,38], in which "*u*" and

"*v*" correlate to the $Ce3d_{3/2}$ and $Ce3d_{5/2}$ spin-orbital multiples, respectively. The peaks referred *v, v*$^{''}$ and *v*$^{'''}$ arise from the multielectron configuration of $3d^94f^2$ ($O\ 2p^4$), $3d^94f^1$ ($O2p^5$) and $3d^94f^0$ ($O2p^6$), which are attributed to the bonding and anti-bongding states of the Ce^{4+} for the $Ce3d_{5/2}$. Additionally, the lines v_0 and *v*$^{'}$ result in the $3d^94f^2$ $O\ 2p^5$ and $3d^94f^1$ $O\ 2p^6$ states of Ce^{3+}. The same peak assignment is also applied to *u* structure, which corresponds to the $Ce3d_{3/2}$. The surface of the sample is not fully oxidized due to the presence of Ce^{4+}/Ce^{3+}, which leads to some oxygen vacancies[34]. It is deduced that Ce-O-Ti bond is formed at the interstitial sites or interfaces between CeO_2 and Ce_2O_3, though their contents are too small to be detected by XRD.

The high-resolution XPS spectra of B1s in the range of 186-197 eV is depicted in Fig.7d. It can be observed that B1s appears at the binding energy 191.73 eV and 192.63 eV. According to the standard binding energy of B1s at 193.1eV (B-O) in B_2O_3 or H_3BO_3 and 187.5eV (B-Ti bond) in TiB_2[39,40], the boron atoms may be incorporated into TiO_2 structure and existing in the form of B-O-Ti or B-O-B structure. Fig.7e displays O 1s high-solution XPS scan spectrum. The broad of O 1s region can be fitted by three peaks, and the peak at 532.9 eV is related to the crystal lattice oxygen (Ti-O), peak at 530.4 eV is attributed to the hydroxyl group (≡Ti-OH) and the peak at 529.0 eV belonged to the bridge oxygen on TiO_2 surface, respectively. Fig.7f shows the XPS spectra of Ti 2p for TNTs and Cu-Ce-B/TNTs. The strong peaks at 458.48 eV and 464.18 eV of Cu-Ce-B/TNTs are assigned to Ti 2p3/2 and Ti 2p1/2, respectively. Compared with pure TNTs (Ti2p3/2 458.48eV and Ti2p1/2 464.18eV),

the intensity decreases and the position of Ti 2p peaks shifts to a higher binding energy due to the presence of Cu, Ce and B in the TiO_2 lattice, which shifts Fermi level of the Cu species (Cu_2O/CuO)[41] and Ce (Ce_2O_3/CeO) compared with that of pure TNTs. Thus, the electrons of TiO_2 may transfer to Cu_2O and CuO, which results in the changes in the outer electron cloud density of Ti, Cu and Ce ions. The Ti2p binding energy therefore increases and Cu2p, Ce3d binding energies decrease. The result suggests that there is an intense interaction between TiO_2 and Cu, Ce species.

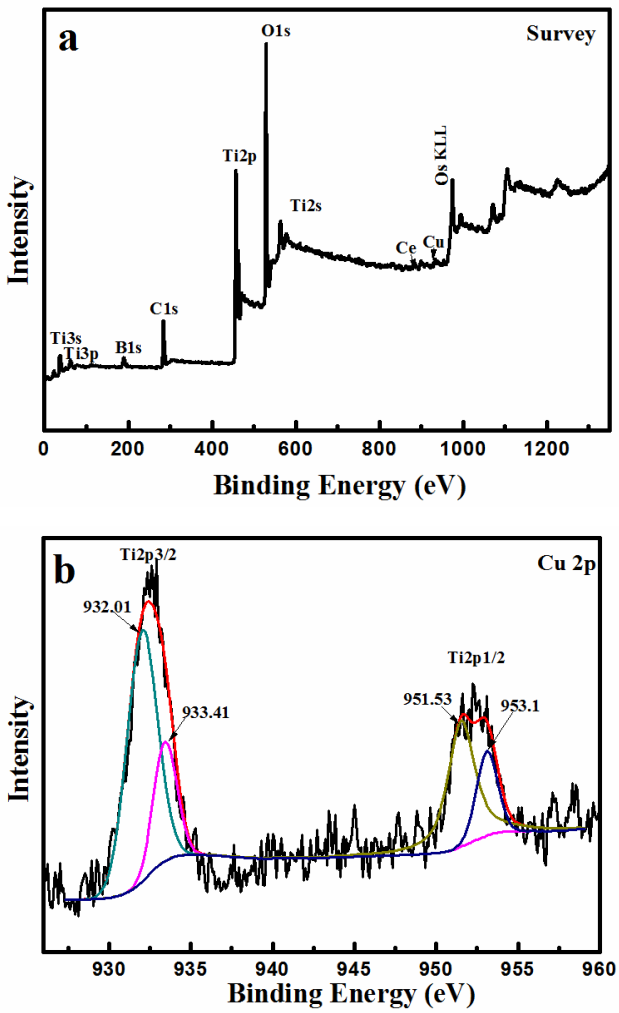

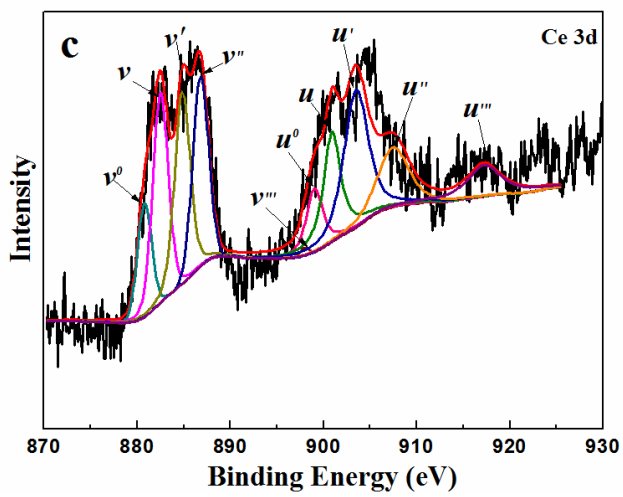

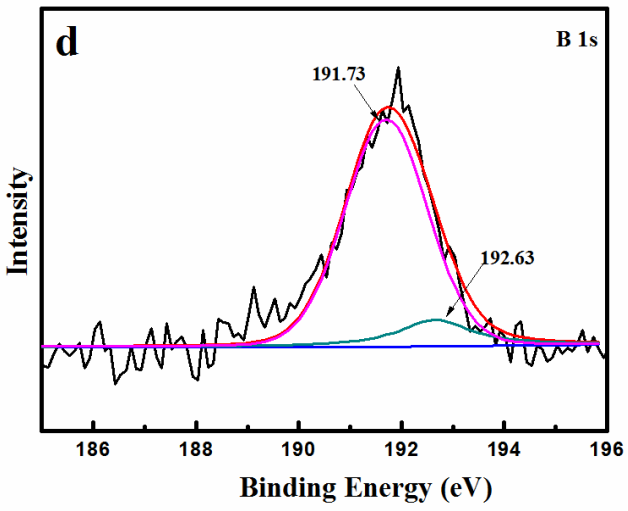

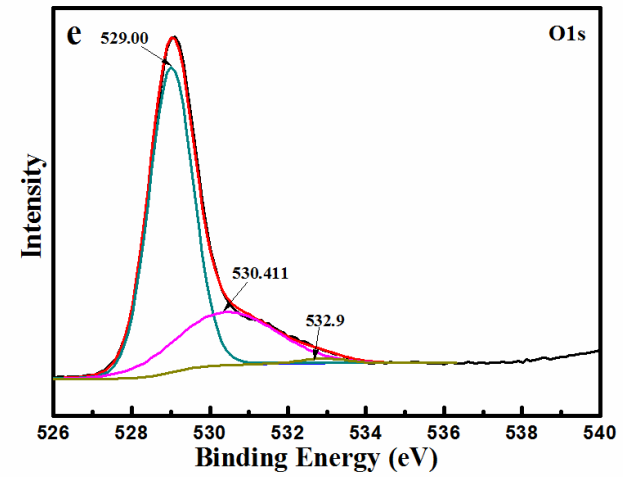

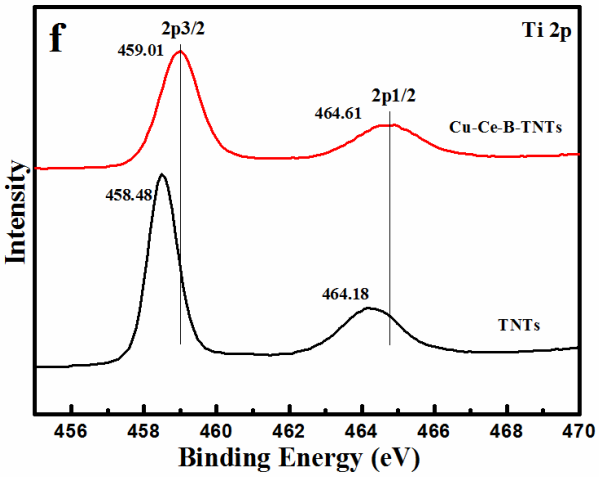

Fig. 7 XPS spectra of Cu-Ce-B/TNTs (a), the high-resolution XPS spectra of Cu2p (b) , Ce3d (c) , B1s (d),O1s (e) , Cu-Ce-B/TNTs and pure Ti2p (f).

3.7 FT-IR analysis

The effect of treating the catalyst before and after the UV irradiation experiments can be observed in Fig.8. In the FT-IR spectra, the curves are much similar except for a peak at 1384.7 cm^{-1}. The broad peaks around 3400 cm^{-1} and 1640 cm^{-1} correspond to the surface-adsorbed water and hydroxyl groups, respectively. Meanwhile, the wide peaks in the range from 1000 cm^{-1} to 500 cm^{-1} are assigned to the bend vibration of Ti-O and Ti-O-Ti bonds. Besides, the peaks at 2852.8 cm^{-1} and 2921.2 cm^{-1} are related to the stretching vibration of C-H. A strong peak at 1384.7 cm^{-1} after reaction indicates that nitrate is accumulated on the surface after photocatalysis[4]. No additional peaks related with Cu, Ce and B appear.

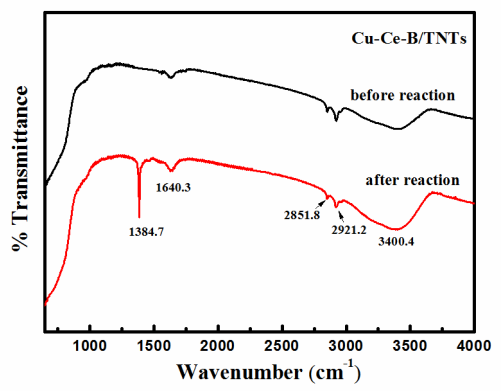

Fig. 8 FT-IR spectra of Cu-Ce-B/TNTs before and after reaction.

3.8 Photocatalytic activities

The photocatalytic activities of all samples in the removal of NO (150 ppm) under UV light were tested, as shown in Fig. 9. Among the all single-doping samples, 0.2 at. % Cu, 0.3 at.% Ce and 2.0 at. % B exhibit the highest photoactivities. According to Fig.9 a(1), it shows that there is rare HNO_2 in late reaction which can be detected. In addition, Fig. 9 b(1) shows that the reaction reach the equilibrium at 20min, then photocatalytic efficiency of the sample began to decrease after 40 min. When it was 60min, the photocatalytic efficiency of the sample is dropped to 64%. However, Fig. 9 c(1) and Fig.9 d(1) shows that the proper humidity is constant at 65% and the TiO_2 nanotubes still have a good photocatalytic activity after washing which indicate the sample has a good recycling rate. The increase of the Cu, Ce and B dose depresses the photoactivity because they could be acts as a center for carrier recombination. Fig. 9d shows that Cu-B, Ce-B, and Cu-Ce co-doped TNTs exhibit higher photocatalytic activity than those of single-doped TNTs, and Cu, Ce and B tri-doped TNTs shows the highest photocatalytic activity due to the synergistic effect of multi-doping. Hybriding of B1s with O2p leads to narrow the valence band (VB),

whereas Ce3d and Cu3d hybriding with Ti3d leads to narrow the conduction band (CB) in the band-gap of TiO_2. Both hybriding events cause the narrowing of the band-gap energy of multi-doped TiO_2. The optical response of multi-doped TiO_2 is increased, leading to an improvement of its photocatalytic activity.

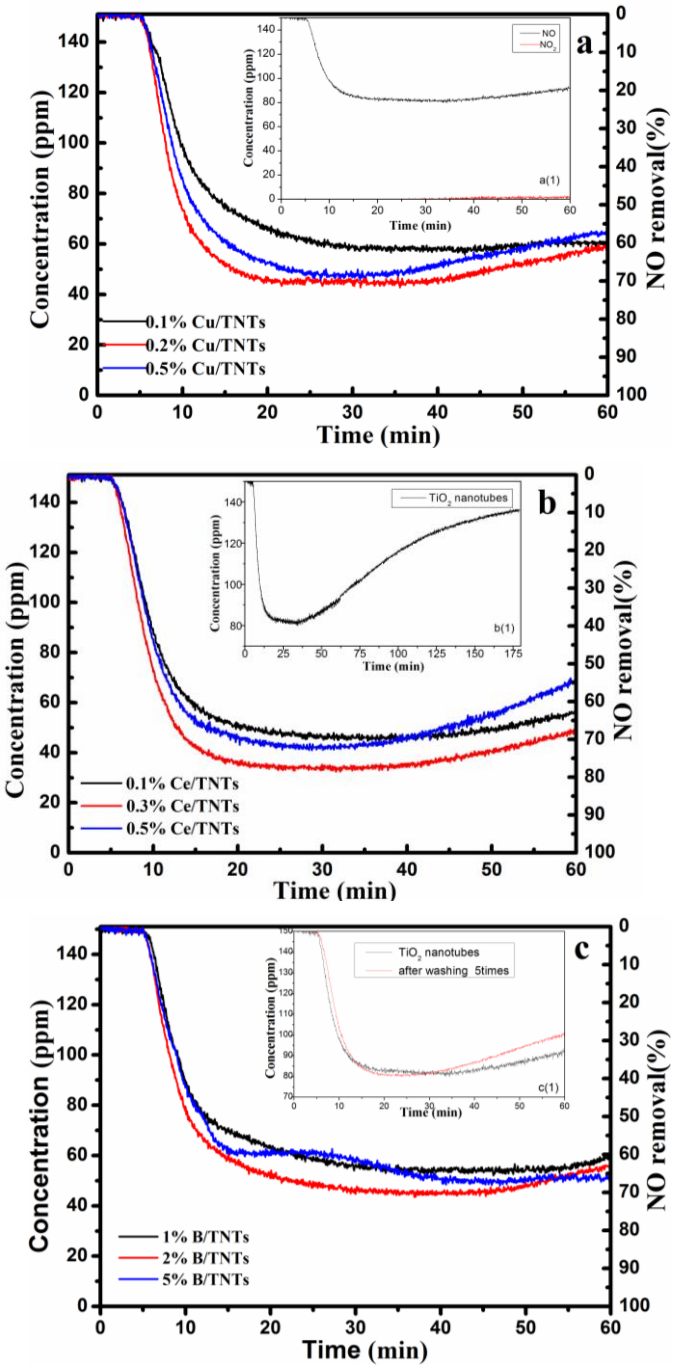

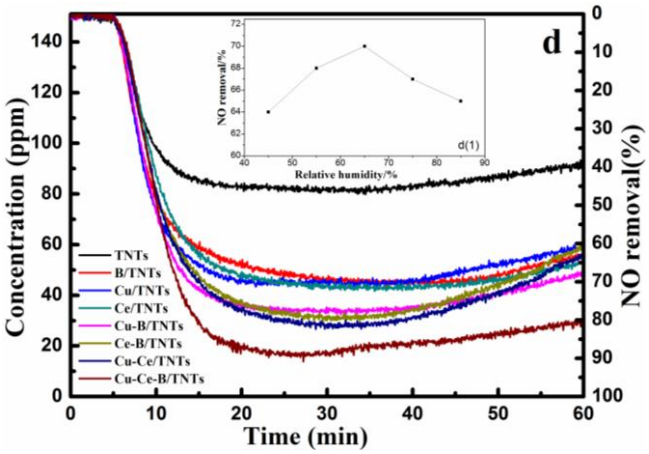

Fig.9 NO removal efficiency of TNTs doped with (a) different amounts of Cu (0.1at%, 0.2at%,0.4at%), a(1) generated NO and NO_2 concentration, (b) different amounts of Ce (0.1at%, 0.3at%,0.5at%), b(1) pure TNTs photocatalytic reaction for 3 hours, (c) different amounts of B (1at%, 2at%, 5at%), c(1) before and after 5 times washing TiO_2 nanotubes, NO removal efficiency of (d) TNTs, B/TNTs, Ce/TNTs, Cu/TNTs, Cu- B/TNTs, Ce-B/TNTs, Cu-Ce /TNTs and Cu-Ce-B/TNTs, d(1) photocatalytic effect of the pure nanotubes at different relative humidity.

3.9 Photocatalytic mechanism

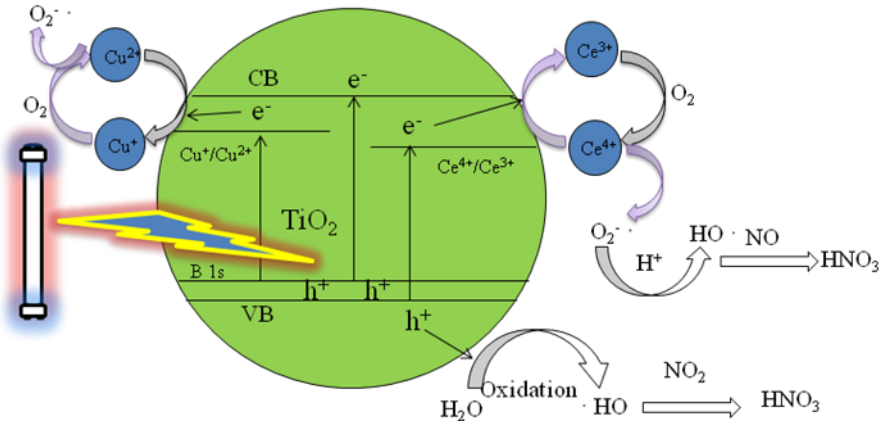

Fig. 10 Schematic illustration of photocatalytic mechanism for Cu-Ce-B/TNTs

Fig.10 shows the schematic illustration of the band energy diagram for the synergetic effect of Cu, Ce, B tri-doped TiO_2-NTs. Copper oxides ($Cu^{2+}/Cu^{+)}$, doping of cerium oxides (Ce^{4+}/Ce^{3+}) and boron into the lattice of TiO_2 will introduce impurity

energy levels in the conduction band (CB) and the valance band (VB), which further narrows the band-gap. Under UV light irradiation, the transfer of excited electrons takes place in several routes. As shown in Fig.10, they can migrate from the B1s impurity level to the conduction band (CB) or can be excited from the valance band (VB) of TiO_2 and the B1s level to the hybridization of Cu^{2+}/Cu^{+} and Ce^{4+}/Ce^{3+} doping energy level, which efficiently inhibits the recombination of photogenerated charge carriers. The reaction contains three main steps as follows:

First, under the illumination by the light of energy greater than the band gap of TiO_2, a part of electrons are excited to the surface and oxide by oxygen, and water reduced by the holes (h^{+});

$$TiO_2 + h\nu \rightarrow e^{-} + h^{+} \quad (2)$$

$$H_2O + h^{+} \rightarrow HO\cdot + H^{+} \quad (3)$$

$$O_2 + e^{-} \rightarrow O_2^{-} \quad (4)$$

Subsequently, the Cu^{2+}/ Ce^{4+} can accept photogenerated electrons as the effective electron trap and reduced to Cu^{+}/Ce^{3+}, simultaneously adsorbs O_2 from the surface to form O_2^{-}, which efficiently separates the recombination of the electrons and holes and thus enhances the photoactivity;

$$Ce^{4+} + e^{-} \rightarrow Ce^{3+} \quad (5)$$

$$Ce^{3+} + O_2 \rightarrow Ce^{4+} + O_2^{-} \quad (6)$$

$$Cu^{2+} + e^{-} \rightarrow Cu^{+} \quad (7)$$

$$Cu^{+} + O_2 \rightarrow O_2^{-} + Cu^{2+} \quad (8)$$

A large amount of the oxygen radicals (O_2^{-}) are obtained from above process,

which are beneficial to photocatalytic process. One of oxygen radicals is reduced hydroxyl free radicals (OH) which can turn NO into NO_3^-, while anther can act as reaction centers directly in removal of NO.

$$H^+ + O_2^- \rightarrow 2HO\cdot \quad (11)$$

$$NO + 2\,HO\cdot \rightarrow NO_2 + H_2O \quad (12)$$

$$NO_2 + HO\cdot \rightarrow NO_3^- + H^+ \quad (13)$$

$$NO + NO_2 + H_2O \rightarrow 2HNO_2 \quad (14)$$

$$NO + O_2^- \rightarrow NO_3^- \quad (15)$$

4. Conclusion

A series of Cu, Ce and B doped TiO_2 nanotubes were successfully synthesized through hydrothermal method assisted CTAB. It was observed that Cu, Ce and B could be intercalated into the interplayer space of nanotubes besides the substitution for the Ti^{4+} or O^{2-}. The photoactivity results show Cu, Ce and B tri-doped TNTs exhibited the highest photoactivity among all as-prepared undoped, single doped and co-doped samples, which should ascribed to a synergetic effect, because B doping induced the formation of new states close to the valence band and conduction bands and shifted of absorption towards visible-light region, while Cu and Ce doping can be efficiently decrease the recombination rate of photogenerated electrons and holes.

Acknowledgements

This work was supported by Fundamental Research Funds for the central universities（HEUCF20151016 and HEUCF20136910012) and Advanced Technique Project Funds of The Manufacture and Information Ministry.

Reference

1 G. Busca, L. Lietti, G. Ramis and F. Berti, *Appl. Catal. B: Environ.*, 1998, **18**, 1.

2 Y. Liu, H. Wang, and Z. Wu, *J. Environ. Sci.*, 2007, **12**, 1505.

3 X. Fan, F. Qiu, H. Yang, W. Tian, T. Hou and X. Zhang, *Catal. Commun.*, 2011, **12**, 1298.

4 L. Chen, J. Li and M. Ge, *Chem. Eng. J.*, 2011, **170**, 531.

5 H. Wang, H. Wang, Z. Wu, Y. Liu and Y. Wang, *Chemosphere*., 2009, **74**, 773.

6 J.M. Bee ŕ, *Prog. Energ. Combust*., 2000, **26**, 301.

7 Q. Chen, H. Liu, Y. Xin, X. Cheng and J. Li, *Appl. Surf. Sci*., 2013, **264**, 476.

8 Z. Wu, H. Wang, Y. Liu, B. Jiang and Z. Sheng, *Chem. Eng. J.*, 2008, **144**, 221.

9 L. Casagrande, L. Lietti, I. Nova, P. Forzatti and A. Baiker, *Appl. Catal. B: Environ.*, 1999, **22**, 63.

10 H. Yan, Z. Q. Tong, B. Wu and J. F. Zhang, *J. Fuel. Chem. Technol.* 2008, **36**, 616.

11 N. H. Nguyen and H. Bai, *J. Environ. Sci.*, 2014, **26**, 1180.

12 Y. Liu, H. Q. Wang and Z. B. Wu, *J. Environ.Sci.*, 2007, **19**, 1505.

13 Y. L. Zou, S. Z. Kang, X. Q. Li, L.X Qin and J. Mu, *Int. J. Hydro. Energ.*, 2014, **xxx**, 1.

14 K. Yang, Y. Dai and B. Huang, *Phys. Rev. B.*, 2007, **76**, 195.

15 W. X. Liu, P. Jiang, W. N. Shao, J. Zhang and W. B. Cao, *Solid. State. Sci.*, 2014, **33**, 45.

16 Y. M. Wu, M. Y. Xing, J. L. Zhang, F. Chen, *Appl. Catal. B: Environ.*, 2010, **97**, 182.

17 J. C. Yu, W. K. Ho, J. G. Yu, H. Y. Yip, P. K. Wong and J. C. Zhao, *Environ. Sci. Technol.* 2005, **39**, 1175.

18 J. Niu, P. Lu, M. Kang, K. Deng, B. Yao, X. Yu and Q. Zhang, *Appl. Surf. Sci.*, 2014, **319**, 99.

19 L. Li, Y. Yang, X. Liu, R. Fan, Y. Shi, S. Li, L. Zhang, X. Fan, P. Tang, R. Xu, W. Zhang, Y. Wang and L. Ma, *Appl. Surf. Sci.*, 2013, **265**, 36.

20 C.Y. Yu and J.C. Yu, *Catal. Lett.*, 2009, **129**, 462.

21 C.L. Yu, L.F. Wei, X. Li, J.C. Chen, Q.Z. Fan and J.C. Yu, *Mat. Sci. Eng. B*, 2013, **178**, 344.

22 C.L. Yu, Q. Shu, C.X. Zhang, Z.P. Xie and Q.Z. Fan, *J.Porous Mater*, 2012, **19**, 903.

23 Y. L. Pang and A. Z. Abdullah, *Appl. Catal. B: Environ.*, 2013, **129**, 473.

24 R. Karla, Reyes-Gil and D. B. Robinson. Acs, *Appl. Mater. Inter.*, 2013, **5**, 12400.

25 N. Pugazhenthiran, S. Murugesana and S. Anandanb, *J. Hazard. Mater.*, 2013, **263**, 541.

26 F. Dong, H. Wang, S. Guo, Z. Wu and S.C. Leed, *J. Hazard. Mater.*, 2011, **187**, 509.

27 X. Yao, X. Zhang, H. Wu, L. Tian, Y. Ma and B. Tang, *Appl. Surf. Sci.*, 2014, **292**, 944.

28 Y. Zhou, D. Shi, H. Li, M. Dang, C. Lu and K. Huang, *Trans. Nonferrous Met. Soc. China.*, 2010, **20**, 2320.

29 S. P. Xu, J. W. Ning, X. W. Zhang, H. W. Bai and D.D. Sun, *Int. J. Hydrogen. Energ.*, 2010, **35**, 5254.

30 Y. Liu, P. Fang, Y. Cheng, Y. Gao, F. Chen, Z. Liu and Y. Dai, *Chem. Eng. J.*, 2013, **219**, 478.

31 N. Yan, Z. Zhu, J. Zhang, Z. Zhao and Q. Liu, *Mate. Res. Bull*, 2012, **47**, 1869.

32 H. H. Ou and S. L. Lo, *Sep. Purif. Technol.*, 2007, **58**, 179.

33 J. Xu, Y. Ao and D. Fu, *Appl. Surf. Sci.*, 2009, **256**, 884.

34 Q. Wang, H. Jiang, S. Zang, J. Li and Q. Wang, *J. Alloy. Compd.*, 2014, **586**, 411.

35 R. Li, G. Chen, J. Dong and X. Sun, *New. J. Chem.*, 2014, **38,** 4684.

36 C. C. Chusuei, M. A. Brookshier and D. W. Goodman, *Langmuir.*, 1999, **15**, 2806.

37 P. Burroughs, A. Hamnett, A. F. Orchard and G. Thornton, *J. Chem. Soc. Dalton Trans.*, 1976, **0**, 1686.

38 A. Galtayries, R. Sporken, J. Riga, G. Blanchard and R. Caudano, *J. Electron. Spectrosc.*, 1998, **88**, 951.

39 M. L. Guo, X. D. Zhang, C. T. Liang, *Physica. B: Condensed Matter.*, 2011, **406**, 3354.

40 L. Deng, B. Zhu, Y. Chen, M. Yao, W. Huang, S. Wang and S. Zhang, *J. Sol-Gel. Sci. Technol.*, 2010, **53**, 535.

41 Q.H. Chen, H.L. Liu, Y. J. Xin and X.W. Cheng, *Chem. Eng. J.*, 2014, **241**, 145.